Journal of Materials Chemistry A

ROYAL SOCIETY OF CHEMISTRY

PAPER

View Article Online
View Journal | View Issue

Cite this: J. Mater. Chem. A, 2025, 13, 11767

A novel approach to describe the electric double layer structure of water-in-salt electrolytes in porous carbon electrodes†

M. Tauhidul Islam, [a] Harald Fitzek,[bc] Bernhard Gollas [a] and Qamar Abbas *[ad]

Understanding the interplay between ion association, desolvation, and electric double layer (EDL) structure is crucial for designing high-performance energy storage devices with concentrated electrolytes. However, these ion dynamics in water-in-salt electrolytes within the nanopores of carbon electrodes are not fully understood. Based on Raman spectroscopy of electrolytes and electrochemical investigations of non-porous electrodes, the classical Gouy–Chapman–Stern model has been modified by incorporating ionicity to estimate the Debye length. The modified model shows a sharp Debye length decrease as the concentration rises from 1 to 10 mol kg^{-1}, followed by an increase due to ion pairing above 10 mol kg^{-1}. The modified model accurately reflects differential and EDL capacitance values obtained from cyclic voltammetry and electrochemical impedance spectroscopy. The data obtained for non-porous electrodes was divided by the MacMullin number (ratio of tortuosity to porosity) of the carbon electrode to estimate the Debye length in the pores. The introduction of the MacMullin number into the Stokes–Einstein equation allowed the estimation of ionic radii within pores, which was subsequently used to calculate the extent of ion desolvation/dehydration in micro- and mesopores. The concentration-dependent ion association governs the Debye length trends in pores, correlating radii of confined ions, ion desolvation, and EDL charging dynamics. Our findings suggest a concentration of 5 mol kg^{-1} LiTFSI as optimal for fastest charging rates and 10 mol kg^{-1} for highest energy density, providing critical insights for developing efficient electrolytes and porous carbon electrodes.

Received 21st January 2025
Accepted 19th March 2025

DOI: 10.1039/d5ta00596e

rsc.li/materials-a

Introduction

Water-in-salt electrolytes exhibit high ionic conductivity, and non-flammability, positioning them as promising sustainable alternatives to organic electrolytes for next-generation energy storage devices such as capacitors and batteries.[1–3] One of the key challenges in harnessing the potential of water-in-salt electrolytes, however, lies in optimizing their concentration. While low electrolyte concentrations may lead to insufficient ion availability and diminished charge storage capacity, excessively high concentrations can result in hindered ion transport, compromising device performance.[4] Sluggish ion transport significantly influences access to subnanometer-size pores,[5] affecting charge/discharge kinetics and power delivery in electrochemical capacitors.[6] As concentration increases, various types of ion pairs emerge,[7–9] limiting ionicity (the ratio of the experimentally obtained molar ionic conductivity to the theoretical molar ionic conductivity calculated using the Nernst–Einstein equation)[5] and charge carrier concentration, which are crucial for achieving high energy densities. Additionally, the compatibility of ionic radii and carbon pore size in electrochemical capacitor electrodes governs ion desolvation, influencing the electrochemical double layer (EDL) structure.[10–15] There is a lack of fundamental knowledge regarding ion electrosorption of water-in-salt electrolytes and their corresponding EDL structure within nanoporous carbon electrodes.

The concept of the EDL began with Helmholtz in 1879,[16,17] who described it as a simple capacitor formed by ions in the electrolyte aligning near a charged surface. In the early 1900s, Gouy and Chapman expanded this idea with the Gouy–Chapman (GC) model, introducing the concept of a diffuse layer where the ions remain mobile and do not adsorb directly onto the charged surface.[18] Instead, the ion distribution within this layer is governed by a balance of electrostatic attraction and thermal motion, where the ion concentration decays exponentially over a distance known as the Debye length. In 1920, Stern combined the Helmholtz and GC models to create the Gouy–Chapman–Stern (GCS) model, which accounts for both an

[a]Institute for Chemistry and Technology of Materials, Graz University of Technology, Stremayrgasse 9, 8010 Graz, Austria. E-mail: qamar.abbas@tugraz.at
[b]Graz Centre for Electron Microscopy, Steyrergasse 17, 8010 Graz, Austria
[c]Institute of Electron Microscopy and Nanoanalysis, Graz University of Technology, Steyrergasse 17, 8010 Graz, Austria
[d]Institute of Chemistry and Technical Electrochemistry, Poznan University of Technology, Berdychowo 4, 60965 Poznan, Poland

† Electronic supplementary information (ESI) available. See DOI: https://doi.org/10.1039/d5ta00596e

immobile Stern layer closest to the electrode surface and a mobile diffuse layer beyond it.[19] However, these classical theories are generally ineffective in describing the electrode–electrolyte interface for concentrated 2 to 10 M aqueous solutions of *e.g.* LiCl, NaCl, and CsCl as has been experimentally demonstrated by Gaddam *et al.*[20] and Smith *et al.*[21]

Most of the earlier models fall short in capturing the intricate interfacial behavior observed in ionic liquids (ILs) due to the interplay of van der Waals, coulombic, dipolar, and solvophobic interactions.[22–24] To this end, Kornyshev and co-workers in 2007 used the Poisson–Fermi equation to model concentrated ionic liquid interfaces employing a mean-field lattice-gas model to derive an analytical expression for the differential capacitance.[25] Around the same time, Bazant *et al.* independently arrived at a similar analytical solution by applying a modified Poisson–Nernst–Planck equation, developing similar expressions for capacitance and potential distribution.[26] Interestingly, Oldham,[27] when adapting the GCS model for IL-electrode interfaces, achieved the same potential profile predictions as those from Goodwin–Kornyshev's mean-field theory in selected scenarios. Recently, Safran and Pincus,[28] and the team of Kornyshev[29,30] demonstrated the effect of ion pairs on the EDL of ILs. In a recent review, Coskun *et al.* mapped the electrode–electrolyte interfaces of ionic liquids and deep eutectic solvents, offering a highly recommended resource for understanding the chronological progress in this field.[23]

Particularly for water-in-salt electrolytes, prior scattering, spectroscopy, and surface force studies have revealed that the EDL comprises both short-range (<10 nm) and long-range (10–50 nm) interfacial layers of ordered ions near the electrode surface.[31–36] McEldrew *et al.* adapted the Poisson–Fermi theory to explain the EDL structure in concentrated LiTFSI using molecular dynamics.[37] However, they ignored the effect of ion-pairing in water-in-salt electrolytes. Moreover, there are limited reports on theories explaining experimental EDL results in bulk water-in-salt solutions. Furthermore, these theories still need to be adapted to adequately explain the EDL structure of water-in-salt electrolytes in carbon pores. Some intricate efforts have been made by Huang *et al.* and Zuliani *et al.* to adapt the GCS model to carbon pores for a wide range of diluted electrolytes.[10–12] These modified models are still limited if the average pore size is close to the size of the solvated or desolvated ions.[38–40] In addition, commercially available carbons usually have pores of different sizes, making it challenging to efficiently probe and differentiate the EDL structure in multiporous carbons using these theories.[6,40,41] Modelling the EDL structure of water-in-salt electrolytes in the porous carbon using Goodwin–Kornyshev's mean-field theory including ion-pairing effects and parameters for pores of different sizes, would lead to a highly complex model with numerous elements.

In addition, ion desolvation/dehydration plays a pivotal role in the charging dynamics of sub-nanometer pores.[42] Understanding the intricate relationships among ion pairing, ion desolvation, and the resulting EDL structure is essential for designing high-performance electrochemical capacitors with water-in-salt electrolytes. *In situ* techniques such as NMR, EQCM, and EQCA are commonly used to investigate desolvation in diluted electrolytes.[14,15,42,43] However, to the best of our knowledge, ion desolvation in water-in-salt electrolytes within carbon pores has not been systematically studied yet.

Furthermore, carbon electrodes often possess a complex architecture with sub-nanometer micro-, meso-, and macropores, which results in sluggish ion transport of water-in-salt electrolyte.[5,6] Slow electrosorption in sub-nanopores present significant challenges for utilizing those mentioned experimental techniques and models to effectively determine and differentiate ion desolvation and the resulting EDL structures within different pores of a multiporous framework.

In this work, we first adapted the Gouy–Chapman–Stern model for bulk water-in-LiTFSI electrolyte by incorporating ionicity into the calculation of the Debye length, *i.e.* the diffuse layer thickness. The trend of the EDL capacitance as a function of the electrolyte concentration using the modified expression for the Debye length closely matches the values obtained from electrochemical impedance spectroscopy (EIS). Likewise, the trend of the diffuse layer thickness aligns with the experimental differential capacitance. We used a commercial carbon containing micro- and mesopores to comprehend the Debye length in the pores. Rather than using complex models,[10–12] we simply divided the Debye length at non-porous electrode by the MacMullin number, *i.e.* the ratio of tortuosity to porosity,[44–46] to differentiate the Debye length distribution in micro- and mesopores. Furthermore, introducing the MacMullin number into the Stokes–Einstein equation enabled the estimation of ionic radii within pores, which was subsequently used to determine ion desolvation in micro- and mesopores. Our findings reveal that ion association governs the Debye length trends in pores, aligning precisely with patterns of confined ionic radii, desolvation, and resulting EDL structure.

Experimental

Lithium bis(trifluoromethanesulfonyl)imide (LiTFSI) was purchased from IoLiTec (Heilbronn, Germany), to prepare a range of electrolytes with concentrations from 0.5 to 20 mol kg^{-1}. For calculating the physicochemical properties of the bulk solutions, the dynamic viscosity (η) was determined with a Modular Compact Rheometer following a standard protocol (MCR 502 SN 82231668 with a cone plate system, Anton Paar, Austria) at room temperature (25 °C). The ionic conductivity, EDL capacitance, and other electrochemical properties were determined in a two-electrode (stainless steel) Swagelok cell using electrochemical impedance spectroscopy (EIS) at open circuit potential (OCP ≈ 30 mV). Cyclic voltammograms (CVs) of the electrolyte solutions were recorded in an electrochemical glass cell configured with three electrodes (glassy carbon as a working electrode) to estimate the differential capacitance. The detailed setup and methodology of EIS and CV are provided in Method S1–S2 and Fig. S1† (ESI†). The ion association patterns in water-in-salt LiTFSI electrolytes were studied by Raman spectroscopy. Raman spectra of the bulk solutions were acquired with a LabRAM HR 800 spectrometer (Horiba, Kyoto, Japan) equipped with a 532 nm laser at a power of 0.5 mW and coupled with an Olympus BX41 microscope. A typical carbon

electrode sheet prepared from multiporous Kuraray activated carbon powder YP80 F was used in the two-electrode symmetric Swagelok-type capacitor cells to investigate the evolution of the EDL structure of water-in-salt LiTFSI electrolytes in the carbon pores, as detailed in Method S3.† The pore configuration of YP80 F was analyzed using nitrogen (N_2) adsorption and desorption at −196 °C with a Micromeritics ASAP 2020 surface area and porosity analyzer (Georgia, U.S.A). The sample was degassed at 140 °C for 12 h, before measuring the isotherm in the relative pressure range of $0.1 < P/P_0 < 1.0$.

Results and discussion

First, we present the electrochemical interfacial characteristics of the LiTFSI electrolytes with non-porous electrodes and discuss the EDL structure based on various theories to demonstrate the different phenomena that occur in water-in-salt LiTFSI systems. We then utilize the properties of the non-porous electrodes to investigate the EDL structure within a multiporous carbon electrode of an electrochemical capacitor cell.

Electrochemical interfacial characteristics of non-porous electrodes in water-in-LiTFSI

The Nyquist impedance plot in Fig. 1a demonstrates an initial decrease in electrolyte resistance with increasing salt concentration, reaching a minimum at 5 mol kg^{-1}. Beyond this concentration, the resistance increases again, becoming progressively higher. This trend indicates that the ionic conductivity of water-in-LiTFSI electrolytes is the result of a specific balance between the number of charge carriers and their mobility. The increasing resistivity observed at salt concentrations above 5 mol kg^{-1} directly indicates ion association, which is discussed in detail in the following section. The low-frequency region is primarily explored here to outline the structure of the interface of a non-porous stainless electrode in water-in-LiTFSI and expressed through a set of electrochemical parameters, which are calculated using eqn (S1)–(S11) as detailed in Method S4.†

The observed impedance behavior, with a tail-like Nyquist plot and the absence of maxima in the plots of imaginary impedance (Z'') (Fig. S2†), real permittivity (ε') (Fig. 1b), and imaginary capacitance (C'') *vs.* frequency (Fig. 1c), indicate the water-in-LiTFSI systems do not have a distinct dielectric relaxation between 1 MHz and 1 mHz, where the capacitive or permittivity properties would significantly change at open circuit potential. The real part of the capacitance of the non-porous electrode also gives no reasonable information (Fig. S3†). Such a phenomenon is typical also for other reported homogeneous diluted electrolytes including KCl and NaCl, where the double-layer capacitance is the primary contributor to the impedance response across the measured frequency range.[47,48]

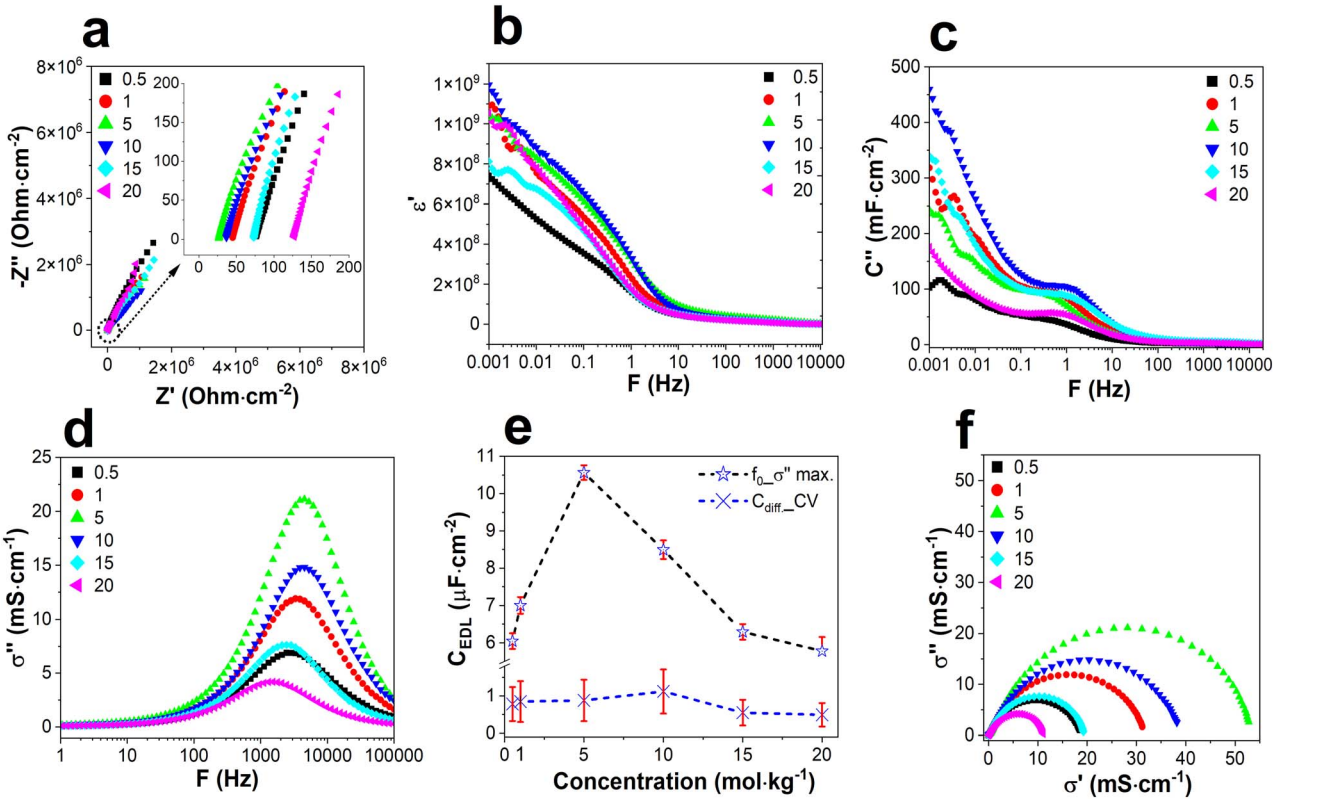

Fig. 1 Concentration-dependent impedance behavior of a non-porous stainless-steel electrode in water-in-LiTFSI electrolytes. (a) Nyquist plot normalized by the geometrical area of electrode (inset shows the magnified high frequency region); (b) real part of permittivity; (c) imaginary capacitance; (d) imaginary ionic conductivity; (e) EDL capacitance from frequency position of the maximum imaginary ionic conductivity and an average of differential capacitance from cyclic voltammograms. The dotted lines serve as a guide to the eye; (f) Cole–Cole conductivity plot.

In this case, representations of conductance (eqn (S8)†) and susceptance (eqn (S9)†) would be insightful,[48] as the major focus of this study is the EDL response. These two quantities are also often termed as real (Y') and imaginary (Y'') parts of admittance (Fig. S4†). Khademi *et al.* compared both equivalent circuit models and admittance for determining the EDL capacitance in NaCl/surfactant mixtures and found similar values.[48] Hence, they recommended utilizing admittance for accurate and direct measurement of capacitance, eliminating the necessity for additional modelling assumptions.[48] However, for broad reader interest, we further normalized the real and imaginary part of admittance with the cell constant to obtain the real (σ') and imaginary (σ'') ionic conductivity from eqn (S10) and (S11),† respectively.[47] Notably, according to these equations, the entire measurement cell is treated as a single capacitor.

In the high-frequency regime, Fig. S5† demonstrates the real part of ionic conductivity as a function of excitation frequency, which corresponds inversely to the trend previously observed in impedance. In all spectra, σ' shows an initial rise with increasing frequency, eventually reaching a plateau in the mid to high-frequency range. As frequency increases, the current begins to bypass the charge transfer resistance through the EDL capacitor.

Moreover, the plateau observed at mid to high frequencies corresponds inversely to the series resistance. In contrast, the key feature of these σ'' spectra (Fig. 1d) is the presence of a characteristic frequency (f_0) at the local maxima, which refers to the charging of the EDL capacitance. This peak shifts towards higher frequencies with increasing LiTFSI concentration until 5 mol kg^{-1}. Beyond this concentration, both σ'' and f_0 decrease, becoming gradually lower towards 20 mol kg^{-1}.

Most likely, at an open circuit voltage of around 30 mV, the stainless-steel rod current collector could be treated as a blocking (non-reactive) electrode. Thus, the f_0 of the σ'' spectrum can be related to EDL capacitance, $C_{EDL,}$ and equivalent series resistance R_S, as expressed in eqn (1). The values of Z' at 1 MHz correspond to R_S.

$$f_0 = \frac{1}{2\pi R_s C_{EDL}} \quad (1)$$

The C_{EDL} obtained using the characteristic frequency method (Fig. 1e) was compared with the differential capacitance derived from cyclic voltammetry. A narrow potential window (Fig. S6†) was chosen for recording the voltammograms to prevent the emergence of cathodic and anodic humps caused by the decomposition of TFSI$^-$.[49] The capacitive current was divided by the scan rate to estimate the average differential capacitance. In an ideal system, capacitive current increases proportionally with the scan rate keeping the differential capacitance constant. However, the currents in CVs of water-in-LiTFSI solutions deviated from such ideal behaviour, probably due to faradaic contributions. This results in a decrease in differential capacitance determined from the voltammetric currents as demonstrated in Fig. S7 and S8.† Therefore, the differential capacitance was determined by averaging the values across five scan rates (10, 20, 50, 100, and 500 mV s^{-1}) at 0 V *versus* SCE (Fig. 1e). The C_{EDL} values were an order of magnitude higher than $C_{diff.}$, reaching a maximum value at 5 mol kg^{-1}. The difference between C_{EDL} and $C_{diff.}$ can be attributed to variations in cell setup, electrochemical methodology, electrode material, and applied potential range. Above this concentration, a declining trend in the capacitance was recorded due to inadequate ion dissociation at these very high concentrations. Based on the above electrochemical characteristics, it is envisioned that quicker polarization, *i.e.* improved charge/discharge rate performance or power performance of the capacitor cell, could be achieved at 5 mol kg^{-1} due to higher permittivity values. Conversely, 10 mol kg^{-1} may be more suitable for delivering higher EDL capacitance and greater energy density.

The following section provides a broader insight into ion-pairing, using several qualitative, configurational, and quantitative approaches to narrate a proper understanding of EDL structure in water-in-salt electrolytes.

Ion pairing in bulk water-in-LiTFSI

To deepen our understanding of the ion association, several Cole–Cole plots were taken into consideration as shown in Fig. S9.† The presence of multiple depressed semicircles in the Cole–Cole permittivity and capacitance plots reveals complex dielectric behavior characterized by multiple relaxation processes and complex ionic environments within the EDL.[50–52] On the other hand, the Nyquist admittance (Fig. S9c†) and Cole–Cole conductivity (Fig. 1f) plots show single perfect semicircles, indicating a single relaxation time and validating the accuracy of our EDL capacitance calculation approach. However, the depressed semicircles in permittivity and capacitance plots provide insights into the extent and nature of ion-pairing in the electrolyte.

The high-frequency semicircle indicates high mobility of free Li$^+$ and TFSI$^-$ and rapid solvent relaxation, with minimal ion pairing. The intermediate-frequency semicircle suggests the presence of loosely bound ion pairs, indicating moderate ion pairing. The low-frequency semicircle reflects the slow dynamics of tightly bound ion pairs or larger complexes, indicative of strong ion pairing or aggregation. The diameter of the semicircle varied as a function of salt concentration, endowing a maximum for 5 mol kg^{-1}, thereby following the trend of ionic conductivity (Fig. 1f). A large diameter signifies a high capacity for charge storage, often due to the presence of free or loosely bound ions, while a small diameter for 15 and 20 mol kg^{-1} indicates lower charge storage capacity, typically due to tightly bound ion pairs.

The influence of ion association on electrochemical data was further confirmed by Raman spectra, showing successive shifts of the sulfur–nitrogen–sulfur (S–N–S) bending band from ~744 cm^{-1} (1 mol kg^{-1}) to ~748 cm^{-1} (20 mol kg^{-1}) as illustrated in Fig. 2a.[53] The LiTFSI salt crystal exhibits an S–N–S band at 751.6 cm^{-1}, as demonstrated in Fig. S10.† This shift results from significant changes in the hydration structure of Li$^+$ and TFSI$^-$, forming various Li$^+$–TFSI$^-$ clusters, such as the free anion (FA) at 738.6 cm^{-1}, the loose ion pair (LIP) at 743.9 cm^{-1}, the intimate ion pair (IIP) at 747.4 cm^{-1}, and the aggregate ion

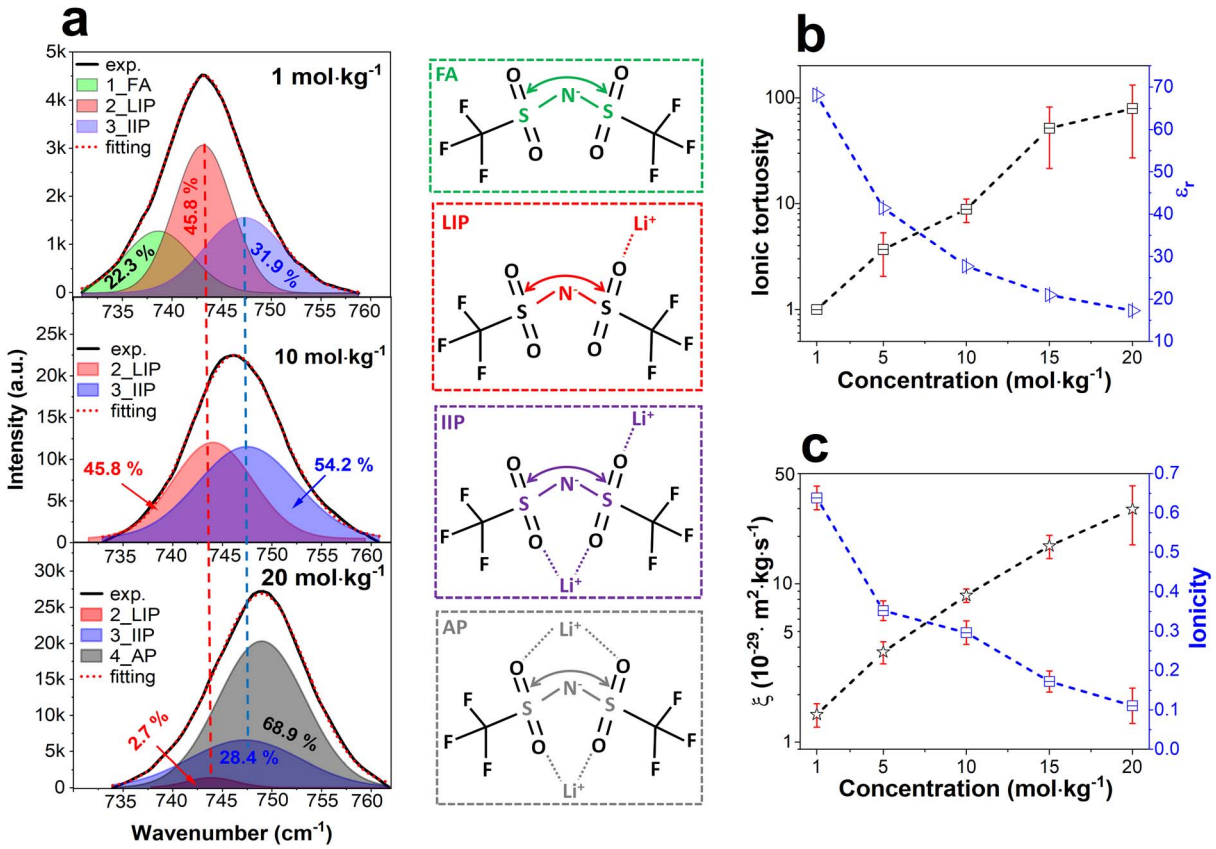

Fig. 2 (a) Raman spectra of 1, 10, and 20 mol kg^{-1} LiTFSI (top to bottom) showing their corresponding free anion, loose ion pair, intimate ion pair, and aggregate ion pair. Vertical red and blue dotted lines indicate the wavenumbers of LIP and IIP. The chemical structures show: the vibration of free TFSI-(FA), the vibration of loosely mono-coordinated TFSI-(LIP), the vibration of loosely/strongly bi-coordinated TFSI-(IIP), the vibration of highly strong bi-coordinated TFSI-(AP); (b) ionic tortuosity and relative permittivity (adopted from ref. 57) of water-in-LiTFSI; (c) inner frictional constant and ionicity of water-in-LiTFSI. The dotted lines in (b) and (c) serve as a guide to the eye.

pair (AP) at 749.1 cm^{-1}. These regions were deconvoluted to estimate the ion-pair contribution percentages based on their corresponding peak area to total area ratio. Peak fitting details along with error ranges are provided in Tables S1 and S2.† At a low concentration of 1 mol kg^{-1}, FA, LIP, and IIP contributions were 22.3%, 45.8%, and 31.9%, respectively. At a moderate concentration of 5 mol kg^{-1}, the FA signature diminished, with LIP and IIP contributions of 45.8% and 54.2%, respectively. At a very high concentration of 20 mol kg^{-1}, AP was the predominant type, contributing 68.9%, with negligible LIP (2.7%) and IIP (28.4%). These values of different ion-pair shares align well with the results of Suo *et al.* as shown in Table S3.[53]†

PFG-NMR shows the co-existence of these ion pairs to result in a dramatic decrease in the diffusivity of Li^+ and $TFSI^-$.[2,7,54,55] The self-ion diffusivity values listed in Tables S4 and S5† were used to obtain ion-pair (mutual) diffusivity values D_{LiTFSI} in Table S6.† This was achieved by applying the modified Darken's relationship for binary diffusivity, as proposed by Krachkovskiy *et al.*[56] and summarized in Method S5. The ionic tortuosity of the water channels imposed by the ion pairs could be expressed as the ratio of diffusivity in the 1 mol kg^{-1} solution to that at any specific concentration between 5 and 20 mol kg^{-1}.[55] Fig. 2b and Table S6† illustrate a notable monotonic increase in ionic tortuosity with respect to salt concentration, aligning with the observations reported by Han *et al.*[55] Therefore, the polarizability of electrolyte solutions decreases with increasing salt concentration, resulting in a very low relative permittivity in Fig. 2b, as determined by Kim *et al.* using dielectric relaxation spectroscopy (fitting parameters).[57]

These spatial phenomena result in a monotonic increase in the inner frictional constant ξ, calculated on the basis of Stokes' law in eqn (2) and illustrated in Fig. 2c.[58]

$$\xi = 8\pi\eta R_H{}^3 \quad (2)$$

Here, η is dynamic viscosity (Table S7†), and RH is the effective hydrodynamic radius. Method S6† summarizes the detailed approach to estimating RH, and values are shown in Tables S8, S9, and S10.†

The higher inner friction ξ eventually decreases progressively the degree of ion dissociation, *i.e.* ionicity (Fig. 2c and Table S7†), producing larger ion-pairing up to ~3.25 nm at 20 mol kg^{-1} (Fig. 3a). The ion-pairing length is also termed as Bjerrum length, l_B, and can be defined by eqn (3).[20,58]

$$l_B = \frac{e^2}{4\pi\varepsilon_r\varepsilon_0 k_B T} \quad (3)$$

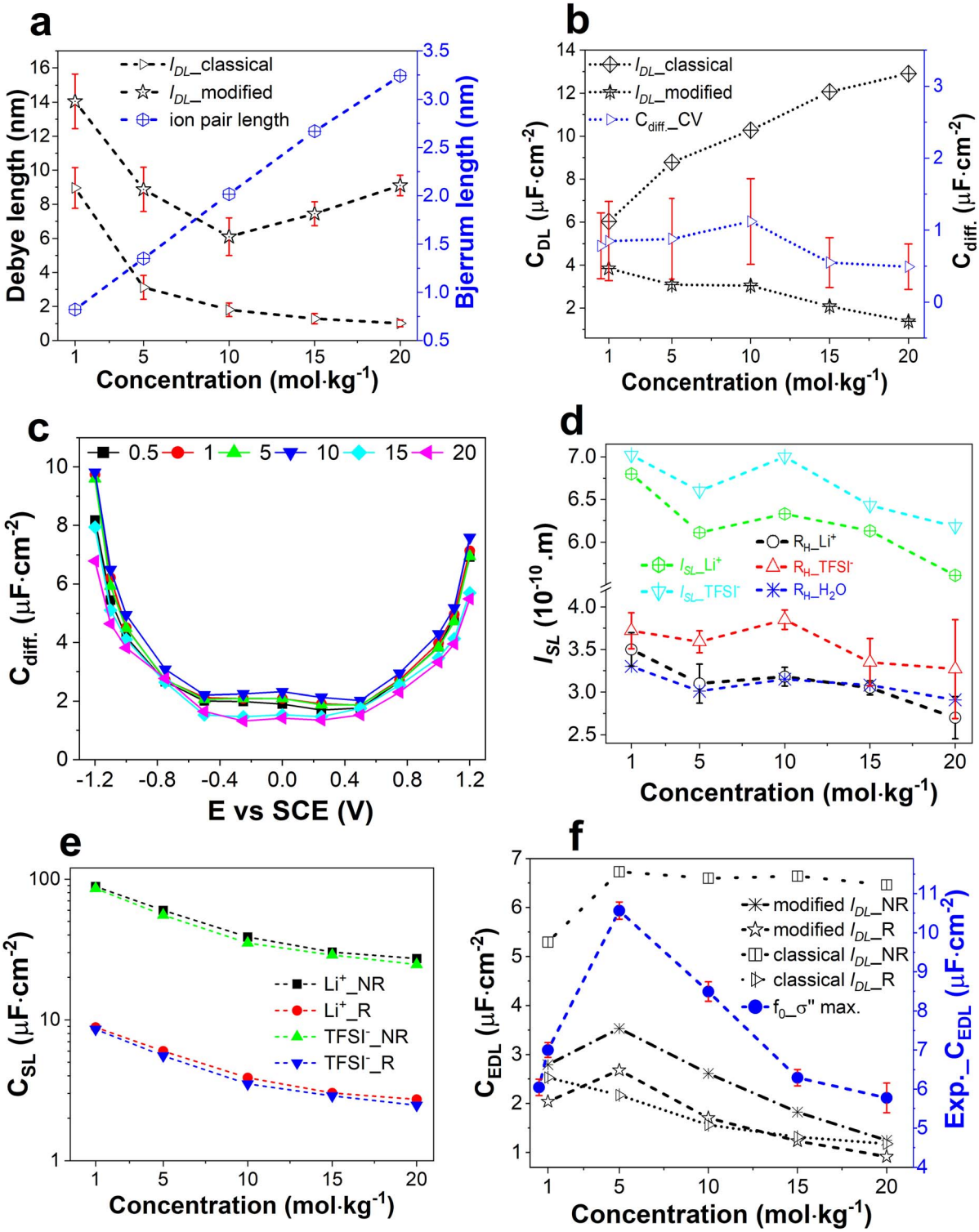

Fig. 3 Salt concentration-dependent (a) Debye length and Bjerrum length of water-in-LiTFSI, (b) theoretical C_{DL} values and experimental differential capacitance, (c) differential capacitance as a function of applied potential *vs.* SCE. These values were taken from the average of anodic and cathodic current at several applied potentials. (d) effective hydrodynamic radii of Li^+, $TFSI^-$, and H_2O and the corresponding Stern layer thickness of Li^+ and $TFSI^-$. A similar range of error bars of R_H values would be also applicable for l_{SL}. To avoid overcrowding error bars were simply excluded. (e) Stern layer capacitance considering both original *i.e.* no-reduction (NR) and 10 times reduction (*R*) of relative permittivity. (f) EDL capacitance considering both reduction and no reduction of relative permittivity. The experimental EDL capacitance from EIS is also shown for comparison. The dotted or solid lines in all figures serve as a guide to the eye.

Here, e is the elementary charge, ε_r is the relative permittivity, ε_0 is the dielectric permittivity of vacuum, k_B is the Boltzmann constant, and T is the temperature. To estimate the ion-pairing length considering the inner friction ξ, we adjusted l_B by incorporating the viscosity and diffusivity using eqn (4).

$$l_B^{eff} = l_B\left(1 + \frac{\eta D}{l_B}\right) \quad (4)$$

The above observations on ion pairing motivated us to incorporate the ion dissociation *i.e.* ionicity values into classical models of diluted solutions to outline the EDL structure in water-in-salt electrolytes as discussed in the following section.

EDL structure of water-in-LiTFSI at non-porous electrodes

In terms of the classical Gouy–Chapman–Stern model (GCS),[48] the overall capacitance of an EDL, C_{EDL}, is the combination of two capacitors in series *i.e.* the Stern layer, C_{SL}, and the diffuse layer, C_{DL}, according to eqn (5).

$$\frac{1}{C_{EDL}} = \frac{1}{C_{SL}} + \frac{1}{C_{DL}} \quad (5)$$

C_{SL} can be calculated using eqn (6), considering the system as an equivalent parallel plate capacitor.

$$C_{SL} = \frac{\varepsilon_{r,SL}\varepsilon_0 A}{l_{SL}} \quad (6)$$

Here, $\varepsilon_{r,SL}$, l_{SL} and A are the relative permittivity of SL, thickness of the SL, and electrode area, respectively. Similarly, for a relatively low potential drop across the diffuse layer, the equivalent C_{DL} can be derived from eqn (7).

$$C_{DL} = \frac{\varepsilon_{r,DL}\varepsilon_0 A}{l_{DL}} \quad (7)$$

Here, $\varepsilon_{r,DL}$ is the relative permittivity of the diffuse layer, which is generally considered to be the same as the bulk permittivity ε_r. This is because the electric field in the diffuse layer is at least one order of magnitude lower than that in the Stern layer.[59,60] In addition, l_{DL} is the approximate diffuse layer thickness of the equivalent parallel plate capacitor, also known as the Debye length, and can be estimated from eqn (8).

$$l_{DL,classical} = \sqrt{\frac{\varepsilon_{r,DL}\varepsilon_0 RT}{2(zF)^2 c}} \quad (8)$$

Here, R, z, F, and c are the universal gas constant, valency, Faraday constant, and bulk electrolyte concentration, respectively.

However, eqn (8) is valid only for diluted solutions. Considering the resulting Bjerrum length ranging in a few nanometers, we introduced the ionicity into eqn (8) to adjust it for water-in-salt electrolytes, as expressed in eqn (9).

$$l_{DL,modified} = \sqrt{\frac{\varepsilon_{r,DL}\varepsilon_0 RT}{2(zF)^2 c}} \cdot \frac{1}{\text{ionicity}} \quad (9)$$

Fig. 3a shows that, according to the classical Debye model, l_{DL} varies with the square root of the inverse ionic strength, *i.e.* the bulk electrolyte concentration.

Consequently, the classical C_{DL} values in Fig. 3b increase proportionally with the square root of the electrolyte concentration. However, the trend of the classical C_{DL} does not match the pattern of experimental differential capacitance in Fig. 3c, resulting in potentially unrealistic values larger by an order of magnitude. In contrast, the modified Debye model shows an initial drop of l_{DL} until 10 mol kg^{-1}.

Beyond this concentration, the l_{DL} shifts to higher values due to a major contribution of larger ion pairs *i.e.* Bjerrum length. Our observed trend and range of the modified l_{DL} align with the findings of the Debye length (~3–10 nm) in various concentrated electrolytes (1–10 M LiCl, 1–5 M NaCl) reported by Gaddam *et al.*[20] and Smith *et al.*,[21] adopting various techniques and models. In addition, the trend of the modified l_{DL} matches the experimental results of various electrochemical properties. A deviation within the same order of magnitude between the modified C_{DL} and experimental differential capacitance is demonstrated in Fig. 3b. However, the trend of the modified C_{DL} does not align with the experimental one. This inconsistency could be due to the significantly declining values of the numerator $\varepsilon_{r,DL}$ *i.e.* relative permittivity of the electrolytes.[57]

In order to determine the EDL capacitance, we still need to estimate the C_{SL}. This is not straightforward, because l_{SL} is not readily available through any direct experimental methods, and there are no ways to deduce the exact $\varepsilon_{r,SL}$ of the Stern layer. However, some approximations were adopted following the propositions of Khademi *et al.*[48] for both the Stern layer thickness and permittivity, which are within the correct order of magnitude.

Since l_{SL} is the closest distance of any hydrated Li^+ or $TFSI^-$ ion to the electrode surface, the summed R_H values of Li^+ and H_2O, and $TFSI^-$ and H_2O were considered for determining the l_{SL} of Li^+ and $TFSI^-$, respectively. The detailed methodology of obtaining R_H of Li^+, $TFSI^-$, and H_2O is discussed in Method S6† and the calculated values are illustrated in Fig. 3d. With increasing salt concentration, l_{SL} was found to decrease from ~7 to 5 Å (Fig. 3d). This range of l_{SL} values is in line with the range ~3 to 10 Å reported in the literature, as obtained using different techniques.[24,31–36,61–63]

The presence of strong electric fields within the Stern layer, even at relatively low potential drops of 10 mV, significantly reduces the permittivity of water due to the reorientation of water molecules and the accumulation of counterions at the electrode surface. This reduction in permittivity of water can vary significantly, ranging from ~78 to 6, influenced by factors such as surface charge density, electrolyte composition, and distance from the surface.[10,11,64]

Hence, we calculate the C_{SL} using both original (Fig. 2e) and tenfold reduced permittivity values to cover a comprehensive range within the correct order of magnitude.[48] Fig. 3e demonstrates the C_{SL} of Li^+ and $TFSI^-$ with (R) and without reduction (NR) of relative permittivity. Li^+ shows a higher C_{SL} due to its smaller R_H and l_{SL} compared to $TFSI^-$. The relative permittivity of 1 mol kg^{-1} and 20 mol kg^{-1} solutions is 68.17 and 17.26,[57]

respectively, resulting in a fivefold decrease in C_{SL} from 1 mol kg^{-1} to 20 mol kg^{-1}. Finally, by combining different C_{DL} and C_{SL} using the GCS eqn (5), the overall C_{EDL} was obtained. Fig. 3f shows the trend of C_{EDL} using the modified l_{DL} matching the experimentally obtained values within the same order of magnitude. This range of C_{EDL} aligns with findings from other experimental and modelling studies, as demonstrated in recent literature review of Schott *et al.*[24] In contrast, using the classical l_{DL}, underestimation of the C_{EDL} was evident, deviating from the experimental trend.

Utilizing the above properties of non-porous electrode, we have extended our study to the EDL structure within a multi-porous carbon electrode of electrochemical capacitor cells as described in the following section.

EDL structure of water-in-LiTFSI confined in carbon nanopores

The MacMullin number (N_M) is a dimensionless quantity used to characterize the ion transport properties of porous media, which can be defined by several parameters as in eqn (10).[44–46]

$$N_M = \frac{R_{bulk}}{R_{pore}} = \frac{\sigma_{bulk}}{\sigma_{pore}} = \frac{D_{bulk}}{D_{pore}} = \frac{\upsilon}{\varnothing} = \frac{l_{DL\ non\text{-}porous}}{l_{DL\ pores}} \quad (10)$$

It provides insight into how the structure of the porous electrode affects the movement of ions within it. Understanding the MacMullin number can help to explain various aspects of the electrochemical behavior of capacitors, including EDL formation, ion transport, and the charge–discharge time constant. The detailed method for obtaining N_M is provided in Method S7.† Related parameters including porosity ($\varnothing$) and tortuosity (υ) were estimated using eqn (S16)–(S24)† with values presented in Fig. 3 and Tables S11 and S12.†[5] Following Landesfeind *et al.*[44] and Xu *et al.*,[45] we recently reported the effective ion diffusivities in micro and mesopores after dividing the bulk electrolyte diffusivity by N_M (Table S12†).[5]

The range of diffusivity aligns with *in situ* PFG NMR studies of organic electrolytes in carbons with different pore sizes.[40,41] We also adopted the similar concept for deriving l_{DL} in pores. Micropores, being smaller in size offer more tortuous networks than mesopores, resulting in higher N_M and smaller l_{DL} values shown in Fig. 4a and b, respectively. With increasing salt concentration, multiple factors shown in Fig. 2 influenced N_M, resulting in a complex trend. In contrast, the l_{DL} values in pores followed a pattern similar to those in the bulk, displaying a minimum at 10 mol kg^{-1}. Our calculated l_{DL} values for micro and mesopores closely match the results (~0.4 to 1.2 nm) obtained with different models such as electric double-cylinder capacitors (EDCC) and electric wire-in-cylinder capacitors (EWCC).[10,11] These EDCC/EWCC models were applied to various activated microporous, mesoporous, templated, and carbide-derived carbons in several aqueous, organic, and ionic liquid-based electrolytes, as reported by Huang *et al.*[11] and Zuliani *et al.*[10]

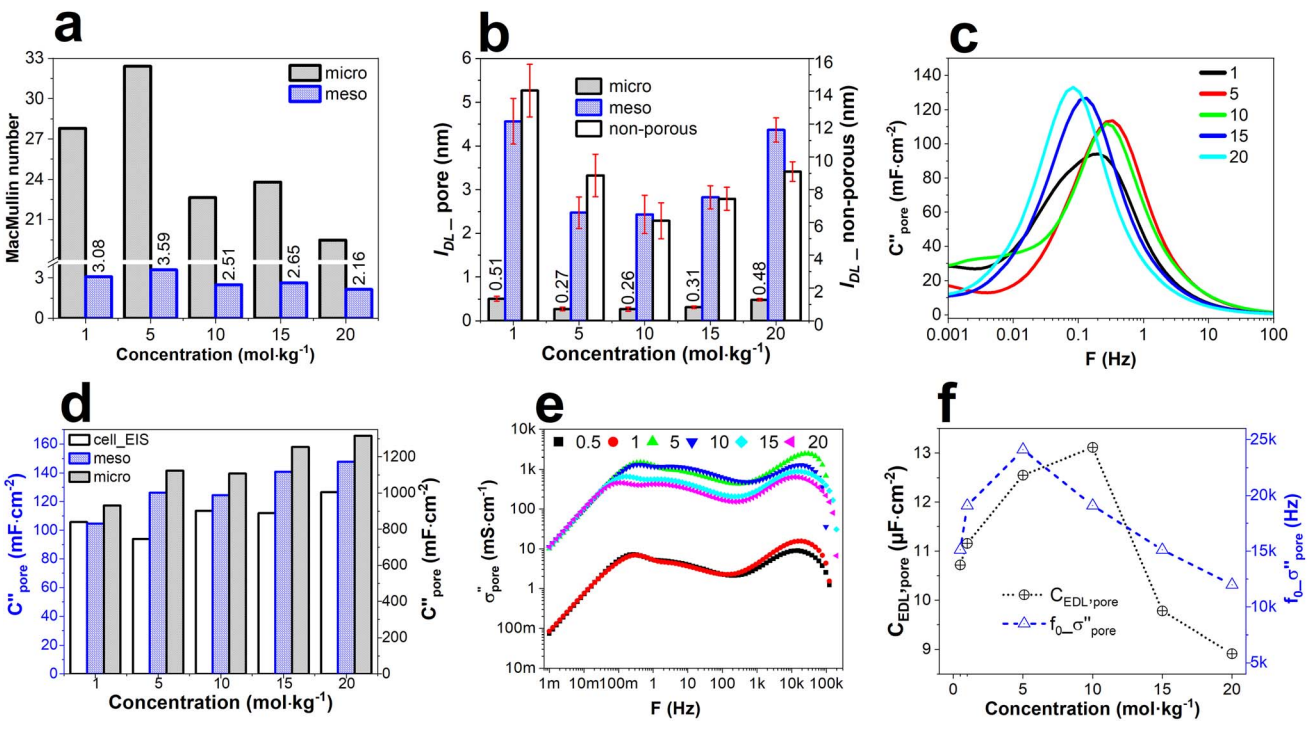

Fig. 4 Properties of porous carbon electrode as a function of salt concentration. (a) MacMullin number of porous carbon sheet used in the electrochemical capacitor cell, (b) Debye length in micro and mesopores and modified Debye length in non-porous electrode, (c) imaginary capacitance C''_{pore} in carbon pore, (d) imaginary capacitance distribution in micro and mesopores along with total cell capacitance from EIS, (e) imaginary conductivity *vs.* frequency plot, and (f) experimental C_{EDL} in pore and the characteristic frequency positions at the maximum σ''_{pore}. The dotted lines serve as a guide to the eye.

In addition, the in-pore l_{DL} values align with the presence of short-range and long-range interfacial layers of ordered ions near the mica electrode surface as demonstrated by Berlinger *et al.* for water-in-salt LiTFSI and $Zn(TFSI)_2$ electrolytes using scattering, spectroscopy, and surface force measurements.[36] The similarity of the values obtained in this work, different reported experiments, and EDCC/EWCC models confirm the accuracy of our approach.

Fig. 4c and d show that the areal C''_{pore} gradually increases up to 10 mol kg^{-1}, matching the trend of the l_{DL} values in pores and ionic resistivity in ion-pores (Table S12†). The higher surface area provides a larger capacitance in micropores than in mesopores. In a similar carbon sheet, these intra-and interconnected pores act as series capacitors. Hence, the reciprocal of micro and mesopore capacitance equals the total experimental capacitance from EIS. At 15 and 20 mol kg^{-1}, however, a further increase in areal C''_{pore} was observed, which is inconsistent with the trend of l_{DL} values in the pores. The gravimetric C''_{pore} in Table S12† also shows the same pattern.

From the trend of l_{DL} values in the pores, we can infer the expected behavior of the diffuse layer capacitance within the pores to double-check the trend of C''_{pore}. According to eqn (7) and the EDCC/EWCC models,[10,11] it can be assumed that the relative permittivity values (Fig. 2b) in the numerator will significantly decrease, while the in-pore l_{DL} in the denominator will concurrently increase at concentrations of 15 and 20 mol kg^{-1} for higher values of the Bjerrum length (Fig. 3a). Therefore, this combined effect will lead to a decrease of in-pore diffuse layer capacitance at these concentrations, analogous to the trend seen for non-porous electrode C_{DL} in Fig. 3b. Similarly, a likely monotonic decline of the Stern layer capacitance within the pores aligns with the non-porous electrode C_{SL}. From this, it can be deduced that the general trend of the theoretical C_{EDL} in the pores reflects the pattern of the l_{DL} in the pores, resulting in a maximum at around 5 or 10 mol kg^{-1}.

In order to verify these theoretical statements, the real (σ'_{pore}) and imaginary (σ''_{pore}) conductivities of the electrochemical capacitor cells were determined using eqn (S10) and (S11),† as shown in Fig. S11† and 4e, respectively. Similar to the non-porous electrode, we determined the EDL capacitance of capacitor cells using eqn (1). The equivalent series resistance (R_S) values were taken from the Nyquist impedance plot of capacitor cells as supplied in Fig. S12.† The characteristic frequency values of eqn (1) were taken from the maximum σ''_{pore} positions in Fig. 4e. With increasing salt concentration, the C_{EDL} values in the pores (Fig. 4f) increased until 10 mol kg^{-1} and then decreased, matching the exact trend of the Debye length in Fig. 4b. The only difference is that the non-porous electrode exhibited a maximum C_{EDL} at 5 mol kg^{-1}. For a better comparison, specific/gravimetric $C_{EDL,in\text{-}pore}$, time constant, and other calculation details are provided in Table S13.† Using EDCC/EWCC models, Huang *et al.* also obtained similar values for the C_{EDL} between ~6 and 16 μF cm^{-2} for various carbons and a wide range of electrolytes.[11] The similarity of theoretical and experimental non-porous and porous electrode's C_{EDL} values in this work confirms the accuracy of our approach to modify the Gouy–Chapman–Stern model by introducing the ionicity. In addition, using the MacMullin number is an easy approach that does not require step-by-step complex approximations. Finally, the imaginary conductivity-based C_{EDL} approximation using eqn (1) provides reliable values without the need for any modeling.

However, the inconsistency between the trend of experimental in-pore C_{EDL} and Debye length with C''_{pore} is due to the dynamic, frequency-dependent nature of EIS. C''_{pore} encompasses a broader range of phenomena, including ion transport, pore structure effects, and non-ideal behavior not captured by the static EDL capacitance alone.

While EDL capacitance measures charge storage capacity at the electrode surface, imaginary capacitance provides insights into the dynamic response of the electrochemical system in a frequency range. For instance, the pattern of C''_{pore} in Fig. 4c indicates that the knee frequency shifts to higher values as salt concentration increases, resulting in a gradually smaller charge/discharge time constant ($1/2\pi f$) up to 5 mol kg^{-1} (440 ms). Above this concentration, the knee frequency shifts to smaller values, resulting in the slowest charge/discharge time at 20 mol kg^{-1} (1256 ms). This trend matches the EDL length in the pores. The larger Bjerrum length (Fig. 3a) and stronger coulombic interactions restrict ion desolvation beyond 10 mol kg^{-1}, resulting in slower charge/discharge rates. To understand this in more depth, the ion desolvation number has been empirically quantified and is discussed in detail in the following section.

Ion-desolvation behaviour of water-in-LiTFSI confined in carbon nanopores

Table S14† indicates that when co-ions and counter-ions are positioned side by side, their size (R_H) range from ~0.597 nm to 0.772 nm, corresponding to ~15% and 49% of the cumulative surface area of micropores <1 nm in YP80 F. This size restricts the mutual transport of ions within the pores. Therefore, partial desolvation/dehydration from the outer shell of the ions is expected within these microporous regions.[41]

To provide deeper insights into partial desolvation, we first determined the radii of ions confined in micropores (eqn (11)) and mesopores (eqn (12)) by combining the Stokes–Einstein equation with the MacMullin number (eqn (10)).

$$D_{micro} = \frac{k_B T}{6\pi\eta R_{H,micro}} \cdot \frac{\varnothing_{micro}}{\mho_{micro}} \quad (11)$$

$$D_{meso} = \frac{k_B T}{6\pi\eta R_{H,meso}} \cdot \frac{\varnothing_{meso}}{\mho_{meso}} \quad (12)$$

Fig. 5a shows the radii of ions confined in micropores and mesopores, along with the radii of bulk ion pairs and sole H_2O (see Method S6 and Tables S8–S10† for details). As salt concentration increases, the number of available water molecules decreases, resulting in a smaller bulk R_H.[55] In the larger mesopores, the ions retain a larger R_H. An initial decline in in-pore radii is observed up to 5 mol kg^{-1}. Beyond 5 mol kg^{-1}, however, the in-pore ionic radii exhibit an opposite trend

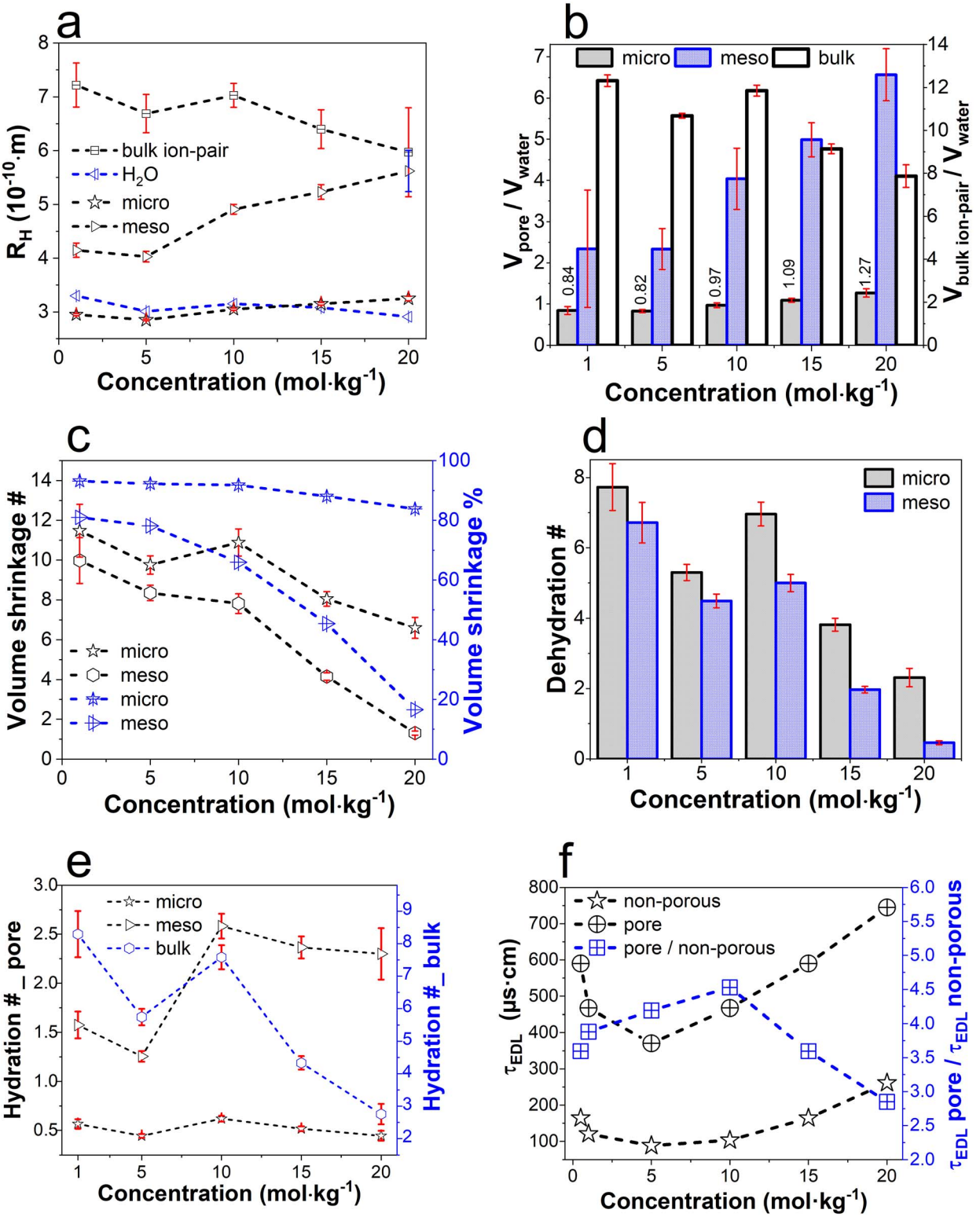

Fig. 5 In-pore hydrodynamic properties related to partial ion desolvation as a function of salt concentration. (a) Radii of ions confined in micro and mesopores as well as bulk ion pair radii and sole water radii, (b) in-pore ion volume to water volume ratio together with bulk ion pair volume to water volume, (c) volume shrinkage number and percentage, (d) partial dehydration/desolvation number in-pore, (e) hydration number in pores and in bulk solution, (f) EDL charging rate of non-porous and porous carbon electrode derived from the time-constant (τ_{EDL}) values of the characteristic frequencies at the maximum σ''_{bulk} and σ''_{pore}. The dotted lines serve as a guide to the eye.

compared to bulk ionic radii, indicating that larger ion-pair sizes restrict partial ion desolvation.

Similar ranges of ionic radii (~3–6 Å) for confined monovalent and divalent ions, including Li^+, were reported by Eliad *et al.*[15] and for $TFSI^-$ (~4–7 Å) by Largeot *et al.*[65] The consistency between our results and these studies confirms the accuracy of eqn (11) and (12). Subsequently, the hydration number N_H of Li^+ and $TFSI^-$ was calculated separately according to eqn (13).[66,67] The N_H values for Li^+ and $TFSI^-$ were then combined to determine the total N_H of LiTFSI, as listed in Table S15.†

$$\mathrm{NH} = \frac{4}{3}\pi\left({R_H}^3 - {R_{CRY}}^3\right) \Big/ V_{water} \quad (13)$$

Here, R_{CRY} is the crystallographic ionic radius and V_{water} is the molecular volume of the water. The R_{CRY} value for Li^+ was borrowed as 0.6 Å from the report of Nightingale,[68] while 3.26 Å for $TFSI^-$ from other ref. 69 and 70 The volume of a water molecule was determined according to Method S8. The hydration numbers in Table S15† indicate that Li^+ ions exhibit strong cosmotropic behavior, forming highly ordered hydration shells due to their high charge density. On the other hand, $TFSI^-$ ions, chaotropic in leading to a less ordered hydration structure. With increasing concentration, the monotonically declining N_H values in bulk solution (Table S15†) align with those reported in other studies.[3]

However, the values of R_H in micropores are smaller than the R_H of individual water molecules (Fig. 5a). Moreover, in some cases, we found that the R_H radii in micropores are smaller than those in the crystalline Li^+-$TFSI^-$ (0.6 + 3.26 = 3.86 Å). Therefore, we could not directly apply eqn (14) and (15) to determine the in-pore hydration number.

$$N_{micro} = \frac{4}{3}\pi\left({R_{H,micro}}^3 - {R_{CRY}}^3\right) \Big/ V_{water} \quad (14)$$

$$N_{meso} = \frac{4}{3}\pi\left({R_{H,meso}}^3 - {R_{CRY}}^3\right) \Big/ V_{water} \quad (15)$$

$$\text{Volume shrinkage\#} = \frac{V_{pore}}{V_{water}} - \frac{V_{bulk}}{V_{water}} \quad (16)$$

$$\text{Volume shrinkage\%} = \frac{\text{volume shrinkage\#}}{\frac{V_{bulk}}{V_{water}}} \quad (17)$$

$$\text{Desolvation\#} = N_{H,bulk} \times \text{volume shrinkage \%} \quad (18)$$

To this end, we adopted a four-step method as summarized in eqn (16)–(18). First, we measured the volume ratio of micro and mesopores to that of water (V_{pore}/V_{water}) and the volume of bulk ion-pairs to that of water ($V_{bulk\ ion\ pair}/V_{water}$) as displayed in Fig. 5b. Second, we subtracted the values of V_{pore}/V_{water} from $V_{bulk\ ion\ pair}/V_{water}$ to achieve the volume shrinkage number and percentage, as demonstrated in Fig. 5c. Third, we multiplied the N_H of bulk LiTFSI from Table S15† by the volume shrinkage percentage to obtain the desolvation number, as revealed in Fig. 5d. Lastly, we subtracted the desolvation numbers from the bulk N_H to determine the hydration numbers in the pores, as shown in Fig. 5e.

Since the above estimation primarily considers ionic volume where the radius of the water molecule significantly affects the results, we utilized four different water volumes.

Firstly, we derived R_H using the diffusivity of H_2O for various LiTFSI concentrations[54] (Method S6†). Secondly, we used the radius of H_2O reported by Han *et al.*[55] Thirdly, we applied a mass and density-based approach (Method S8). Lastly, we considered the water radius to be 3 Å.[48] Fig. 5b–e display average values derived from these four different radii. To ensure accurate estimations, we utilized effective hydrated radii throughout our work.

This was achieved by correcting the Stokes radii from the Stokes–Einstein equation using the calibration plot of Nightingale (Method S6†).[63] The resulting range of hydration numbers in pores (N_H ranging from ~0.05 to 6) is in good agreement with previous reports on various electrolytes, including Li_2SO_4 and LiCl, confined in several nanoporous carbons (YP-17, BP-880, BP-2000) determined using electrochemical quartz crystal admittance (EQCA) and electrochemical quartz crystal microbalance (EQCM) methods.[13,14,43]

Fig. 5b–e summarize the behavior of LiTFSI ions during electrosorption, focusing on changes in hydrodynamic volume in micro- and mesopores. Mesopores, being larger, retain a smaller surface area for ionic volume sieving, resulting in approximately fivefold less partial desolvation than in micropores. Ion desolvation is stronger at lower concentrations due to factors related to ion–water interactions and electrolyte structure. At lower concentrations, more water molecules are available relative to the number of ions, allowing each ion to be fully solvated with strong hydration shells. These shells are partially stripped off during electrosorption in the narrow spaces of micro- and mesopores, which leads to greater desolvation of the ions (Scheme 1a). Additionally, the strong hydration shells around ions like cosmotropic Li^+ contribute to efficient charge screening, resulting in lower Debye lengths (decreasing from 1 to 10 mol kg^{-1}). As these ions move towards porous carbon electrode surfaces during electrosorption, the hydration shells are partially removed to facilitate closer interactions between ions and pore walls. At lower concentrations, the relative dielectric constant is also higher (*e.g.* 68.17 at 1 mol kg^{-1}),[57] which supports stronger interactions between ions and solvents. This forces ions to lose part of their hydration shell to fit into narrow sub-nanopores, increasing hydrodynamic volume shrinkage and partial ion desolvation. In contrast, as the concentration increases to 15 and 20 mol kg^{-1}, ion pairing becomes more prominent. This pairing reduces the ionicity and the relative permittivity of the solution (*e.g.* 17.26 at 20 mol kg^{-1}),[57] thereby decreasing the hydrodynamic volume and desolvation number within micro- and mesopores. At these concentrations, the formation of EDL is hindered, because the reduced permittivity and increased ion pairing decrease effective ion distribution and charge storage. Larger ion pairings are less easily accommodated in sub-nanosized carbon pores, limiting the ion distribution and sorption characteristics within the pores (Scheme 1b).

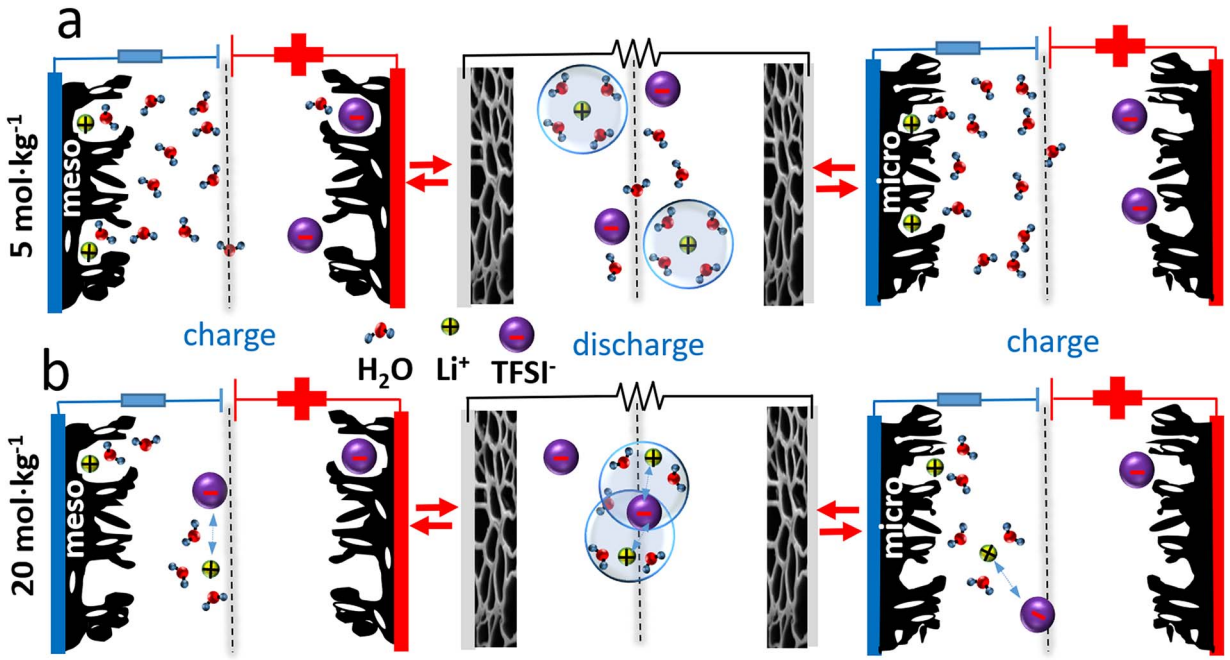

Scheme 1 The EDL structure and ion-desolvation behavior under discharged (all sub-nanopores) and charged (micro and mesopores) conditions in porous carbon electrodes differ significantly between (a) 5 mol kg^{-1} and (b) 20 mol kg^{-1} LiTFSI concentrations. Mesopores accommodate more charges than micropores, but ion desolvation is more pronounced in micropores. At 5 mol kg^{-1}, the presence of free $TFSI^-$ and loosely bound ion pairs allows for efficient charge screening. In contrast, at 20 mol kg^{-1}, the stronger coulombic interactions within intimate and aggregated ion pairs hinder dissociation, resulting in a greater Debye length and sluggish charge screening.

The ratio of hydration numbers from bulk to pore could serves as an indicator of ion hydration/desolvation ability at varying concentrations. For micropores, the ratios were 14.66, 12.93, 12.25, 8.39, and 6.20, while for mesopores, they were 5.27, 4.57, 2.94, 1.83, and 1.20 at 0.5, 1, 5, 10, 15, and 20 mol kg^{-1}, respectively. The monotonic decline in these values indicates that with increasing concentration, ion pairs stabilize partially dehydrated states, as ions bound in pairs are less likely to disrupt their hydration shells (Scheme 1b). Consequently, the extent of ion desolvation is governed by the strength and type of ion pairing, with stronger pair interactions promoting reduced solvation and limiting further desolvation within pores. As a result, electrosorption dynamics shift, with high concentrations leading to less structured ion sorption and potentially reduced charge storage efficiency. The strong hydration and structuring effects of cosmotropic Li^+ ions are counteracted by the chaotropic nature of $TFSI^-$ ions, leading to a complex interplay that influences the overall performance of the electrolyte in electrochemical capacitors. Hence, moderate concentrations, such as 5 and 10 mol kg^{-1}, demonstrated better charge screening performance. Except for C_{EDL} from σ''_{bulk}, the Debye length minima, C_{EDL} from σ''_{pore}, differential capacitance from CVs, and other theoretical C_{EDL} values were higher at 10 mol kg^{-1}. This is attributable to the higher desolvation number compared to 5 mol kg^{-1}.

In other words, up to 10 mol kg^{-1}, the decreasing Debye length suggests strong hydration shells around Li^+ ions, facilitating effective charge screening and enhancing electrosorption efficiency.

Above 10 mol kg^{-1}, the coexistence of intimate and aggregated ion pairs results in Bjerrum lengths of 2.5 and 3.5 nm for 15 and 20 mol kg^{-1}, respectively, which are larger than the micropores (≤2 nm) (Fig. 3a). This results in a smaller diffuse layer thickness in porous carbon, as shown in Fig. S14,† derived from the loss tangent plot (Method S9). To correlate the ion pairing and desolvation phenomena with the EDL charging rate, we derived the time-constant (τ_{EDL}) from the characteristic frequency positions at the maximum σ''_{bulk} and σ''_{pore} using eqn (19), as shown in Fig. 5f and listed in Table S16.†

$$\tau_{EDL} = \frac{1}{2\pi f''_{\sigma}} \cdot \frac{A}{d} \quad (19)$$

As previously described in Methods S1 and S2,† the σ''_{bulk} and σ''_{pore} were obtained using cells with different cell constants. According to the Helmholtz equation (Method S4†), we accounted for the electrode area and distance (for bulk solution) or carbon sheet thickness (for capacitor cells) in eqn (19). Due to varying tortuosities in micro and mesopores across different salt concentrations, the time-constants for EDL charging of the pores were significantly higher than in non-porous electrodes, differing by several orders of magnitude. For example, a 5 mol kg^{-1} concentration resulted in short τ_{EDL} both for non-porous (88.4 μs cm) and porous (370.54 μs cm) electrodes, whereas a 20 mol kg^{-1} concentration led to large τ_{EDL} both for non-porous (261.4 μs cm) and porous (744.8 μs cm) electrodes. The pore-to-non-porous EDL charging time-constant ratios were 3.6, 3.8, 4.2, 4.5, 3.6, and 2.8 for 0.5, 1, 5, 10, 15, and 20 mol kg^{-1}

concentrations, respectively. This concentration-dependent trend exactly follows the patterns of Debye length and ion desolvation, showing a maximum at 10 mol kg^{-1}. Borchardt *et al.* described the ion diffusivity ratio from bulk to in-pore as ion transport resistance.[41] Similarly, the τ_{EDL} ratio of porous to non-porous electrodes can be considered as an indicator of EDL charging readiness. The peak τ_{EDL} porous/τ_{EDL} non-porous at 10 mol kg^{-1} suggests the highest charge accumulation, signifying the formation of a compact and efficient EDL at this concentration. These findings indicate that a 10 mol kg^{-1} concentration is better suited for maximizing EDL capacitance and achieving higher energy density (determined using Method S10 and shown in Fig. S15†). Conversely, the time-constants derived from the maximum imaginary conductivity, capacitance, power, and loss tangent (Table S16†) suggest that a 5 mol kg^{-1} concentration may be more favorable for faster EDL charge/discharge rates, resulting in higher power density (determined using Method S11 and presented in Fig. S16†).

Conclusions

Ion dissociation in water-in-salt LiTFSI plays a key role in determining charge/discharge rates of nanoporous carbon electrode. Ionic association is influenced by the electrolyte concentration giving rise to various types of ion pairs which determine the EDL structure by influencing the Debye length. Thus, correct Debye Length estimation in water-in-salt electrolytes requires the ionicity to be incorporated in Gouy–Chapman–Stern model, whose accuracy is validated *via* similarity between models and experimental EDL capacitance values of non-porous and porous electrodes. Using the MacMullin number proved to be a straightforward approach, avoiding complex approximations for the Debye length in and outside of pores. Moreover, the use of imaginary conductivity-based EDL capacitance approximation from EIS provides reliable results without the need for additional models. Experimental C_{EDL} values from imaginary conductivity, differential capacitance from CVs, and other theoretical C_{EDL} values were higher at 10 mol kg^{-1}, likely due to the higher desolvation number compared to 5 mol kg^{-1}. Beyond 10 mol kg^{-1}, the presence of intimate and aggregated ion pairs resulted in Bjerrum lengths of 2.5 nm and 3.5 nm for 15 mol kg^{-1} and 20 mol kg^{-1}, respectively, exceeding the size of micropores ($\leq$2 nm). These pairs stabilize partially desolvated states, as ions bound in pairs are less likely to disrupt their hydration shells, thereby limiting further desolvation in pores. This limitation leads to inefficient charge screening. From these findings, we discern that a concentration of 5 mol kg^{-1} LiTFSI is optimal for achieving fast charge/discharge rates and high power density. Whereas, strong coulombic interactions within intimate and aggregated ion pairs hinder dissociation at high concentrations, resulting in an enhanced Debye length and sluggish charge screening.

List of symbols

A	Geometric area of the electrode
c	Bulk electrolyte concentration
C'	Real part of capacitance
C''	Imaginary part of capacitance
C_0	Capacitance of ideal capacitor in vacuum
C_{EDL}	Electric double layer capacitance
C_{SL}	Capacitance in Stern layer
C_{DL}	Capacitance in diffuse layer
$C_{diff.}$	Differential capacitance
C'_{pore}	Real part of capacitance in pore
C''_{pore}	Imaginary part of capacitance in pore
C_{DL}	Capacitance in diffuse layer
C''_{micro}	Imaginary part of capacitance in micropore
C''_{meso}	Imaginary part of capacitance in mesopore
d	Distance between electrodes
D	Diffusivity
D_{LiTFSI}	Mutual ion diffusivity of bulk Li^+-$TFSI^-$
D_{micro}	Effective ion diffusivity in micropores
D_{meso}	Effective ion diffusivity in mesopores
e	Elementary charge
E	Applied potential
f	Frequency
ε'	Real part of permittivity
ε''	Imaginary part of permittivity
ε_0	Permittivity in vacuum
ε_r	Relative permittivity
$\varepsilon_{r,SL}$	Relative permittivity in Stern layer
$\varepsilon_{r,DL}$	Relative permittivity in diffuse layer
N_M	MacMullin number
N_H	Hydration number
N_{micro}	Hydration number in micropore
N_{meso}	Hydration number in mesopore
P	Power of electrochemical capacitor
σ'	Real part of ionic conductivity
σ''	Imaginary part of ionic conductivity
σ'_{bulk}	Real part of ionic conductivity in bulk electrolyte
σ'_{pore}	Real part of ionic conductivity in carbon pore
σ''_{bulk}	Imaginary part of ionic conductivity in bulk electrolyte
σ''_{pore}	Imaginary part of ionic conductivity in carbon pore
R	Universal gas constant
R_H	Effective hydrodynamic ionic radius
R_{CRY}	Crystallographic ionic radius
$R_{in\text{-}pore}$	Ionic resistance in carbon electrode
R_{micro}	Ionic resistance in micropore
R_{meso}	Ionic resistance in mesopore
R_S	Equivalent series resistance
η	Viscosity
ξ	Inner frictional constant
$\varnothing$	Porosity
$\mho$	Tortuosity
$\mho_{micro}$	Tortuosity in micropore
$\mho_{meso}$	Tortuosity in mesopore
T	Temperature
τ	Charge–discharge time-constant
τ_{EDL}	EDL charging time-constant
tan δ	Dielectric loss tangent
ω	Angular frequency
V_{water}	Molecular volume of the water molecule
V_{bulk}	Hydrodynamic ionic volume in bulk electrolyte

V_{pore}	Hydrodynamic ionic volume in carbon pore
Y'	Real part of admittance or conductance
Y''	Imaginary part of admittance or susceptance
z	Valency
Z'	Real component of the impedance
Z''	Imaginary component of the impedance

List of abbreviations

AP	Aggregated ion pair
CV	Cyclic voltammogram
EIS	Electrochemical impedance spectroscopy
EDL	Electric double layer
EDCC	Electric double-cylinder capacitors
EWCC	Electric wire-in-cylinder capacitors
FA	Free anion
GCS	Gouy–Chapman–Stern
IIP	Intimate ion pair
LIP	Loose ion pair
OCP	Open circuit potential

Data availability

The data supporting the results of this study have been included in the ESI,† and additional data are available from the corresponding authors upon reasonable request.

Author contributions

MTI: conceptualization; data curation; formal analysis; investigation; methodology; software; validation; visualization; writing – original draft. HF: Raman experiments, investigation, writing – review & editing. BG: supervision; writing – review & editing, project administration; resources. QA: conceptualization; supervision; funding acquisition; project administration; resources; writing – review & editing.

Conflicts of interest

The authors have no financial and personal relationships with other people or organizations that could inappropriately influence their work.

Acknowledgements

The Austrian Research Promotion Agency (FFG) is thankfully acknowledged for funding this research under the ECOCAPs project # 39966764.

Notes and references

1 M. Amiri and D. Bélanger, *ChemSusChem*, 2021, **14**, 2487–2500.
2 Q. Abbas, P. Nürnberg, R. Ricco, F. Carraro, B. Gollas and M. Schönhoff, *Adv. Energy Sustainability Res.*, 2021, **2**, 2100115.
3 L. Suo, O. Borodin, T. Gao, M. Olguin, J. Ho, X. Fan, C. Luo, C. Wang and K. Xu, *Science*, 2015, **350**, 938–943.
4 P. Lannelongue, R. Bouchal, E. Mourad, C. Bodin, M. Olarte, S. le Vot, F. Favier and O. Fontaine, *J. Electrochem. Soc.*, 2018, **165**, A657–A663.
5 M. T. Islam, B. Gollas and Q. Abbas, *J. Mater. Chem. A*, 2024, **12**, 25504–25518.
6 G. Moreno-Fernández, R. Mysyk, N. Díez, D. Carriazo and J. M. López del Amo, *Electrochim. Acta*, 2022, **404**, 139716.
7 O. Borodin, L. Suo, M. Gobet, X. Ren, F. Wang, A. Faraone, J. Peng, M. Olguin, M. Schroeder, M. S. Ding, E. Gobrogge, A. Von Wald Cresce, S. Munoz, J. A. Dura, S. Greenbaum, C. Wang and K. Xu, *ACS Nano*, 2017, **11**, 10462–10471.
8 D. W. McOwen, D. M. Seo, O. Borodin, J. Vatamanu, P. D. Boyle and W. A. Henderson, *Energy Environ. Sci.*, 2014, **7**, 416–426.
9 D. M. Seo, P. D. Boyle, R. D. Sommer, J. S. Daubert, O. Borodin and W. A. Henderson, *J. Phys. Chem. B*, 2014, **118**, 13601–13608.
10 J. E. Zuliani, C. Q. Jia and D. W. Kirk, *J. Phys. Chem. C*, 2017, **121**, 20555–20566.
11 J. Huang, B. G. Sumpter and V. Meunier, *Chem.–Eur. J.*, 2008, **14**, 6614–6626.
12 J. Huang, B. G. Sumpter and V. Meunier, *Angew. Chem.*, 2008, **47**, 520–524.
13 Z. Bo, J. Yang, H. Qi, J. Yan, K. Cen and Z. Han, *Energy Storage Mater.*, 2020, **31**, 64–71.
14 M. D. Levi, S. Sigalov, G. Salitra, R. Elazari and D. Aurbach, *J. Phys. Chem. Lett.*, 2011, **2**, 120–124.
15 L. Eliad, G. Salitra, A. Soffer and D. Aurbach, *J. Phys. Chem. B*, 2001, **105**, 6880–6887.
16 H. Helmholtz, *Ann. Phys.*, 1853, **7**, 353–377.
17 H. Helmholtz, *Ann. Phys.*, 1879, **243**, 337–382.
18 D. L. Chapman, *Philos. Mag.*, 1913, **25**, 475–481.
19 O. Stern, *Z. Elektrochem. Angew. Phys. Chem.*, 1924, **21–22**, 508–516.
20 P. Gaddam and W. Ducker, *Langmuir*, 2019, **35**, 5719–5727.
21 A. M. Smith, A. A. Lee and S. Perkin, *J. Phys. Chem. Lett.*, 2016, **7**, 2157–2163.
22 Y. A. Budkov and A. L. Kolesnikov, *Curr. Opin. Electrochem.*, 2022, **33**, 100931.
23 O. K. Coskun, M. Muñoz, S. Dongare, W. Dean and B. E. Gurkan, *Langmuir*, 2024, **40**, 3283–3300.
24 C. M. Schott, P. M. Schneider, K.-T. Song, H. Yu, R. Götz, F. Haimerl, E. Gubanova, J. Zhou, T. O. Schmidt, Q. Zhang, V. Alexandrov and A. S. Bandarenka, *Chem. Rev.*, 2024, **124**, 12391–12462.
25 A. A. Kornyshev, *J. Phys. Chem. B*, 2007, **111**, 5545–5557.
26 M. S. Kilic, M. Z. Bazant and A. Ajdari, *Phys. Rev.*, 2007, **E75**, 021503.
27 K. B. Oldham, *J. Electroanal. Chem.*, 2008, **613**, 131–138.
28 S. A. Safran and P. A. Pincus, *Soft Matter*, 2023, **19**, 7907–7911.
29 Z. A. H. Goodwin, M. McEldrew, J. P. De Souza, M. Z. Bazant and A. A. Kornyshev, *J. Chem. Phys.*, 2022, **157**, 094106.
30 Z. A. H. Goodwin and A. A. Kornyshev, *Electrochim. Acta*, 2022, **434**, 141163.

31 T. Ichii, S. Ichikawa, Y. Yamada, M. Murata, T. Utsunomiya and H. Sugimura, *Jpn. J. Appl. Phys.*, 2020, **59**, SN1003.
32 R. Zhang, M. Han, K. Ta, K. E. Madsen, X. Chen, X. Zhang, R. M. Espinosa-Marzal and A. A. Gewirth, *ACS Appl. Energy Mater.*, 2020, **3**, 8086–8094.
33 M. Han, R. Zhang, A. A. Gewirth and R. M. Espinosa-Marzal, *Nano Lett.*, 2021, **21**, 2304–2309.
34 Y. Zhang, N. H. C. Lewis, J. Mars, G. Wan, N. J. Weadock, C. J. Takacs, M. R. Lukatskaya, H.-G. Steinrück, M. F. Toney, A. Tokmakoff and E. J. Maginn, *J. Phys. Chem. B*, 2021, **125**, 4501–4513.
35 T. S. Groves, C. S. Perez-Martinez, R. Lhermerout and S. Perkin, *J. Phys. Chem. Lett.*, 2021, **12**, 1702–1707.
36 S. A. Berlinger, V. Küpers, P. J. Dudenas, D. Schinski, L. Flagg, Z. D. Lamberty, B. D. McCloskey, M. Winter and J. Frechette, *Proc. Natl. Acad. Sci. U. S. A.*, 2024, **121**(31), e2404669121.
37 M. McEldrew, Z. A. H. Goodwin, A. A. Kornyshev and M. Z. Bazant, *J. Phys. Chem. Lett.*, 2018, **9**, 5840–5846.
38 C. Prehal, C. Koczwara, N. Jäckel, A. Schreiber, M. Burian, H. Amenitsch, M. A. Hartmann, V. Presser and O. Paris, *Nat. Energy*, 2017, **2**, 16215.
39 A. C. Forse, C. Merlet, J. M. Griffin and C. P. Grey, *J. Am. Chem. Soc.*, 2016, **138**, 5731–5744.
40 A. C. Forse, J. M. Griffin, C. Merlet, J. Carretero-Gonzalez, A. R. O. Raji, N. M. Trease and C. P. Grey, *Nat. Energy*, 2017, **2**, 16216.
41 L. Borchardt, D. Leistenschneider, J. Haase and M. Dvoyashkin, *Adv. Energy Mater.*, 2018, **8**, 1800892.
42 Z. X. Luo, Y. Z. Xing, S. Liu, Y. C. Ling, A. Kleinhammes and Y. Wu, *J. Phys. Chem. Lett.*, 2015, **6**, 5022–5026.
43 M. D. Levi, S. Sigalov, D. Aurbach and L. Daikhin, *J. Phys. Chem. C*, 2013, **117**(29), 14876–14888.
44 J. Landesfeind, J. Hattendorff, A. Ehrl, W. A. Wall and H. A. Gasteiger, *J. Electrochem. Soc.*, 2016, **163**, A1373–A1387.
45 J. H. Xu, T. Schoetz, J. R. McManus, V. R. Subramanian, P. W. Fields and R. J. Messinger, *J. Electrochem. Soc.*, 2021, **168**, 060514.
46 N. Ogihara, Y. Itou and S. Kawauchi, *J. Phys. Chem. Lett.*, 2019, **10**, 5013–5018.
47 L. F. Lima, A. L. Vieira, H. Mukai, C. M. G. Andrade and P. R. G. Fernandes, *J. Mol. Liq.*, 2017, **241**, 530–539.
48 M. Khademi and D. P. J. Barz, *Langmuir*, 2020, **36**, 4250–4260.
49 W. Giurlani, L. Sergi, E. Crestini, N. Calisi, F. Poli, F. Soavi and M. Innocenti, *J. Solid State Electrochem.*, 2022, **26**, 85–95.
50 M. E. Orazem and B. Tribollet, *Electrochemical Impedance Spectroscopy*, John Wiley & Sons, Inc, Hoboken, NJ, 2008.
51 F. Kremer, A. Schönhals and W. Luck, *Broadband Dielectric Spectroscopy*, Springer-Verlag, Berlin, Heidelberg, 1st edn, 2003.
52 J. Zhao, Q. Lei, F. He, C. Zheng, Y. Liu, X. Zhao and J. Yin, *ACS Appl. Polym. Mater.*, 2019, **1**, 2862–2874.
53 L. Suo, D. Oh, Y. Lin, Z. Zhuo, O. Borodin, T. Gao, F. Wang, A. Kushima, Z. Wang, H. C. Kim, Y. Qi, W. Yang, F. Pan, J. Li, K. Xu and C. Wang, *J. Am. Chem. Soc.*, 2017, **139**, 18670–18680.
54 Z. Li, R. Bouchal, T. Mendez-Morales, A. L. Rollet, C. Rizzi, S. Le Vot, F. Favier, B. Rotenberg, O. Borodin, O. Fontaine and M. Salanne, *J. Phys. Chem. B*, 2019, **123**, 10514–10521.
55 K. S. Han, Z. Yu, H. Wang, P. C. Redfern, L. Ma, L. Cheng, Y. Chen, J. Z. Hu, L. A. Curtiss, K. Xu, V. Murugesan and K. T. Mueller, *J. Phys. Chem. B*, 2020, **124**, 5284–5291.
56 S. Krachkovskiy, M. Dontigny, S. Rochon, C. Kim, M. L. Trudeau and K. Zaghib, *J. Phys. Chem. C*, 2020, **124**, 24624–24630.
57 J. Kim, B. Koo, J. Lim, J. Jeon, C. Lim, H. Lee, K. Kwak and M. Cho, *ACS Energy Lett.*, 2022, **7**, 189–196.
58 Z. Abdollahi, M. T. Darestani, S. Ghasemi and V. G. Gomes, *Colloid Polym. Sci.*, 2014, **292**, 2695–2705.
59 F. Booth, *J. Chem. Phy.*, 1951, **19**, 391–394.
60 H. Wang, J. Varghese and L. Pilon, *Electrochim. Acta*, 2011, **56**, 6189–6197.
61 I. C. Bourg, S. S. Lee, P. Fenter and C. Tournassat, *J. Phys. Chem. C*, 2017, **121**, 9402–9412.
62 M. A. Brown, Z. Abbas, A. Kleibert, R. G. Green, A. Goel, S. May and T. M. Squires, *Phys. Rev.*, 2016, **X6**, 011007.
63 A. Velikonja, E. Gongadze, V. Kralj-Iglič and A. Iglič, *Int. J. Electrochem. Sci.*, 2014, **9**, 5885–5894.
64 E. Gongadze and A. Iglič, *Bioelectrochemistry*, 2012, **87**, 199–203.
65 C. Largeot, C. Portet, J. Chmiola, P. L. Taberna, Y. Gogotsi and P. Simon, *J. Am. Chem. Soc.*, 2008, **130**, 2730–2731.
66 Y. Matsuda, H. Nakashima, M. Morita and Y. Takasu, *J. Electrochem. Soc.*, 1981, **128**, 2552–2556.
67 N. G. Tsierkezos and A. I. Philippopoulos, *Fluid Phase Equilib.*, 2009, **277**, 20–28.
68 E. R. Nightingale, *J. Phys. Chem.*, 1959, **63**, 1381–1387.
69 Y.-J. Kim, Y. Matsuzawa, S. Ozaki, K. C. Park, C. Kim, M. Endo, H. Yoshida, G. Masuda, T. Sato and M. S. Dresselhaus, *J. Electrochem. Sci.*, 2005, **152**, A710.
70 N. Q. Khuyen, Z. Zondaka, M. Harjo, J. Torop, T. Tamm and R. Kiefer, *Polymers*, 2019, **11**, 849.